

Better than a lens

A novel concept to break the SNR-limit, given by Fermat's principle.

Jan Becker¹, Ronny Förster¹ and Rainer Heintzmann^{1,2,3*}

¹ *Leibniz Institute of Photonic Technology, Albert-Einstein Str. 9, 07745 Jena, Germany*

² *Institute of Physical Chemistry, Friedrich-Schiller-University Jena, Helmholtzweg 4, 07743 Jena, Germany*

³ *Abbe Center of Photonics, Friedrich-Schiller-University Jena, Albert-Einstein Str. 6, 07745 Jena, Germany*

** corresponding author: heintzmann@gmail.com*

KEY WORDS: incoherent imaging, photon noise, signal-to-noise ratio (SNR), pupil splitting, weighted averaging

Abstract

The signal in an incoherent imaging system gets transferred worse towards higher spatial frequencies. Since the photon noise is distributed equally in Fourier space, the signal-to-noise ratio (SNR) decreases, and therefore represents a fundamental limit in the field of imaging. Our work aims to go beyond this given SNR-limit, which is directly connected to circumvent Fermat's principle (1662). The proposed technique only makes use of a single acquisition process. To our knowledge this hasn't been done before and might have far-reaching impact on a large number of applications ranging from bio-imaging to industrial inspection. Especially in the case of limited photon numbers, e.g. fluorescent emission or a minimum available detector exposure time (temporal resolution), our method represents a new way to improve on SNR, which has been missing so far.

We propose a novel and fundamentally new concept, by splitting the pupil of an imaging system into two parts to simultaneously obtain sub-images via each of these sub-pupils. Since the noise variance is proportional to the number of detected photons, it has been reduced in each of the sub-images. Recombining them by weighted averaging in Fourier-space yields an enhancement in (Fourier-) SNR compared to conventional imaging, enabling us to break the aforementioned SNR-limit. This results in an increased effective resolution limit in real space, which is used as an indicator throughout this work.

We show a proof-of-concept experiment, in which we split the pupil by displaying orthogonally oriented blazed phase gratings for the different sub-pupils on a phase-only spatial light modulator. Our experiment confirms the improvement in effective resolution and therefore shows that we have overcome the fundamental SNR-limit, by only manipulating the captured light distribution in the pupil plane.

Basic principles of imaging

Lenses have been around for many hundred years and well proven their qualities in forming images of objects ranging from galaxies to single molecules. But are they always the best choice for the task at hand?

There is a good reason that lenses are so commonly used. A lens is designed to interfere all rays passing through it constructively at its nominal focus (*Fermat's principle*, first mentioned in 1662 [1]). This very definition guarantees the maximal concentration of light at the focal spot and therefore yields a physical limit that cannot be overcome. In this work we will introduce an idea how to circumvent this limit in a computational way, without the need to capture several images sequentially or increase illumination power. Hence our method proves to be useful for imaging scenarios with a limited number of photons, where no alternative exists so far.

We consider a standard telecentric incoherent imaging system (e.g. a $4f$ -system, as given in an infinity corrected microscope; f being the focal length) as given by two lenses spaced at such a distance that their

focal planes coincide (Fig. 1 a). Such a system is characterized by assuming a pupil stop in the Fourier plane, limiting the maximum angle (limits the numerical aperture NA , independent of the object position) under which the imaging system is capable of relaying light from the sample $S(\vec{r})$ to the image $I(\vec{r})$. With \vec{r} denoting the position. Without loss of generality, we assume unit magnification (same focal length for both lenses) and scalar theory obeying the Abbe sine condition [2] (results of vectorial calculations are additionally shown in supplement S8 and confirm our findings).

Incoherent image formation can be approximated in Fourier space as a simple product [3]:

$$\tilde{I}(\vec{k}) = \tilde{S}(\vec{k}) \tilde{h}(\vec{k}) \quad (1)$$

with the Fourier-transform being indicated by a tilde \sim above the respective quantity and \vec{k} denoting a spatial frequency vector. $\tilde{h}(\vec{k})$ is the optical transfer function (OTF) corresponding to the Fourier-transformation of the point spread function (PSF), $h(\vec{r})$.

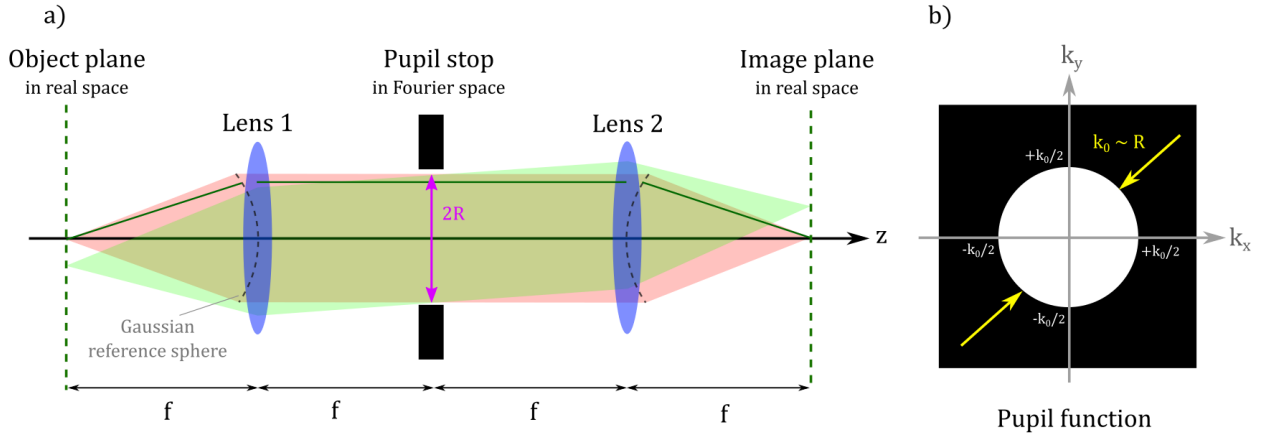


Figure 1 | 4f-imaging system and its corresponding pupil function. a) Optical imaging setup with two lenses placed such that their focal planes coincide. The system's pupil (line in magenta) is located in the Fourier plane, related via the Gaussian reference spheres to the sine of the angle to the axis [1]. b) The two dimensional shape of the pupil transmission function ($\tilde{a}(\vec{k}) \in \mathbb{C}$; white/black = 100 / 0 % transmission) is a scaled version of the physical pupil. Its radius R is proportional to the system's cut-off frequency k_0 .

According to eq. (1), the value of the OTF describes how well spatial frequencies of the object are preserved in the imaging process. It is important to note that this function is only non-zero for spatial frequencies below a well-defined cut-off frequency k_0 (the Abbe-limit [4]), set by the system's pupil stop radius R (see Fig. 1 a).

The performance of an optical imaging system is described by its pupil function ($\tilde{a}(\vec{k}) \in \mathbb{C}$), a scaled version of the physical pupil stop (see Fig. 1 b). Such a pupil allows a modification of the amplitude and phase distribution of the light. It is thus interesting to ask, given a physically limited pupil, which $\tilde{a}(\vec{k})$ is optimal for an imaging task at hand.

Due to the intensity PSF being the squared magnitude of the amplitude distribution, the OTF is obtained [3] as the autocorrelation of the pupil function:

$$\tilde{h}(\vec{k}) = \mathcal{A}\{\tilde{a}(\vec{k})\} = \int_{\mathbb{R}^3} \tilde{a}(\Delta\vec{k})^* \tilde{a}(\Delta\vec{k} + \vec{k}) d\Delta\vec{k} \quad (2)$$

with the star denoting the complex conjugate of $\tilde{a}(\Delta\vec{k})$.

Considering a full pupil (FP) in the scalar *paraxial* case, this leaves us with the conventional OTF $\tilde{h}_{FP}(k_r)$ as shown in Fig. 2 a) (blue crosses) with the radial spatial frequency k_r .

The autocorrelation, can be visualized as quantifying how many result frequency vectors \vec{k} fit into the pupil (red arrows Fig. 2 a). This is given by the blue area, which decreases with growing \vec{k} (details in S1) explaining the loss of contrast towards higher spatial frequencies in an incoherent imaging system.

Note that any reduction in pupil transmittance or phase alteration only leads to local reductions in the OTF but never an increase. Hence, a clear pupil seems to perform best in terms of signal transmission independent of spatial frequency.

The influence of noise

However, having established this, there is still a catch: light is also a particle. It is usually measured by counting the number of photons that are detected. We are assuming to have an ideal detector (neglecting dark & readout noise, additionally see Discussion) and identify photon noise to be characteristic of the measured photon flux, and not to be some particular detector property.

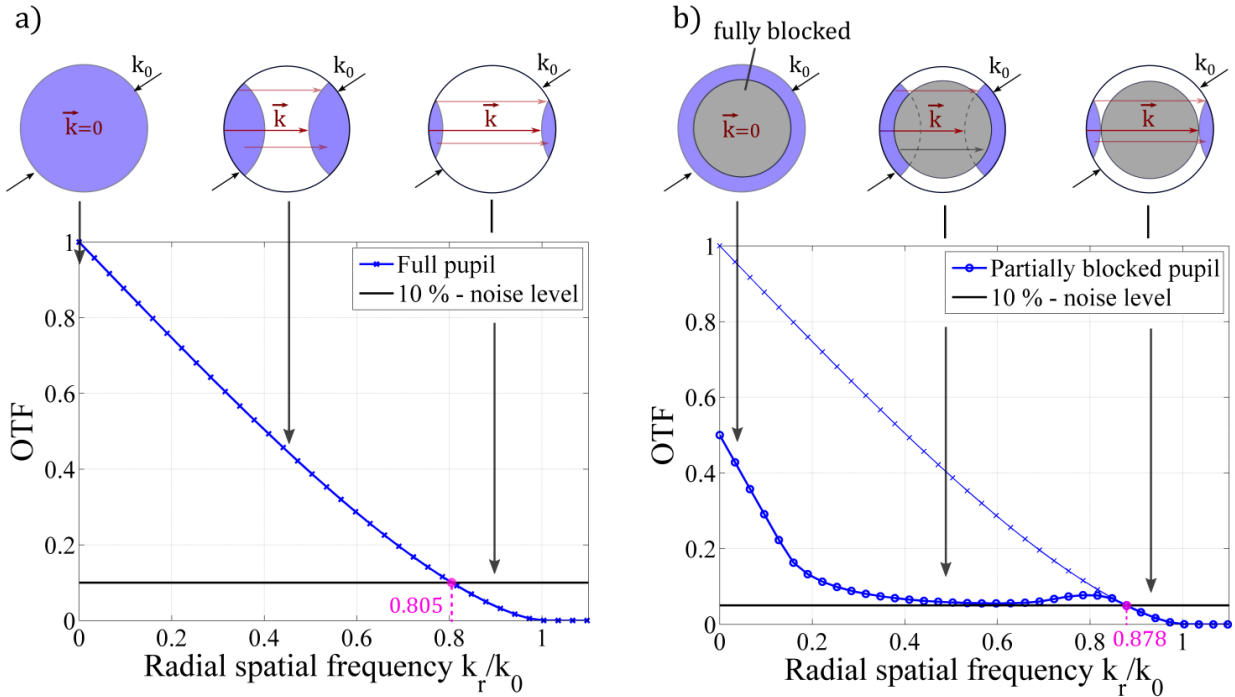


Figure 2 | Graphical construction of the incoherent OTF for to a given pupil. *Top:* autocorrelation of the pupil visualized as a quantifying difference vectors (c.f. S1). *Bottom:* OTF as a function of radial spatial frequency k_r/k_0 . **a)** A full pupil leads to the FP-OTF (blue crosses). The area (top, blue) spanned by a given difference vector (red arrows) corresponds to the OTF strength at this frequency. Photon noise in Fourier space is uniform over spatial frequencies (bottom, black solid line). An effective resolution limit is estimated by the magenta point (assuming 10 % noise), which is the crossing point of the OTF and the noise floor. It is an indicator for the fundamental SNR-limit, and is used later to indicate its exceeding. **b)** Blocking a central region (gray inner circle) leads to a better SNR performance for high \vec{k} , where the blue area has not been reduced (top, outermost graphic) but the overall transmission is lowered. The effective resolution limit has thus been increased (in this example by $\approx 9\%$) as the new OTF (blue circles) intersects the noise floor closer to the cut-off frequency.

So it is worth revisiting the above statement with photon noise in mind, i.e. assuming Poisson-distributed values of I_r , with the index r referring to the image intensity pixel. Note that we have switched to a *discrete* notation, to emphasize that we work with image data (a discrete quantity). In the case of photon-limited noise, the expectation value $\langle I_r \rangle = \mu_r$ is equal to the variance $Var\{I_r\}$ [5], denoted by μ_r :

$$Var\{I_r\} = \langle I_r \rangle = \mu_r \quad (3)$$

Thus the noise is signal dependent (can vary in real space) and therefore fewer photons cause less noise.

Because photon noise is uncorrelated in real space, the variance in Fourier space (sum of variances of real and imaginary part, see eq. S 5) is uniform (white noise) [6]. The variance is given by the total number of expected photons, as derived in S2 (pre-factors of the Fourier transform have been omitted):

$$\text{Var}\{\tilde{I}_k\} = \sum_r \mu_r = \text{const.} \quad \forall k \quad (4)$$

This noise level is depicted in Fig. 2 as the solid black line and defines an effective resolution limit (magenta dot), which is given as the intersection of the OTF (blue crosses) with the uniform noise floor. It is a direct indicator of the fundamental SNR-limit, and is used to demonstrate its exceeding. The 10% noise as shown in Fig. 2 corresponds to an average of 100 photons per pixel, yielding an improvement in terms of effective resolution of $\approx 9\%$ (given as the relative difference of magenta dots).

Revisiting the correlation argument, changing phases of the pupil will still only lower the height of the OTF with no effect on the photon noise. However, changing the transmittance of the pupil plane mask reduces the total number of transmitted photons, and thus decreases the variance of the photon noise at **all** spatial frequencies. Hence the SNR in Fourier space increases (see S2) if the OTF transmission remains unchanged:

$$\text{SNR}_k = \frac{|\tilde{I}_k|}{\sqrt{\text{Var}\{\tilde{I}_k\}}} = \frac{|\tilde{I}_k|}{\sqrt{\sum_r \mu_r}} \quad (5)$$

The absolute value is taken to ensure a strictly real-valued result.

Figure 2b) shows this effect for a circular obstruction (gray area) in the center of the pupil. Blocking this part of the pupil will reduce the OTF-value (reduction of blue area) for medium spatial frequencies, because not every difference vector from the FP still fits into the modified pupil (gray arrow in middle graphic at the top of Fig. 2 b).

However, close to the cut-off frequency there is no overlap of the blocked (gray) and the transfer (blue) areas (top right, Fig. 2b). Hence the signal transfer is the same as in the FP case (compare the two OTFs). Yet, the noise floor is reduced by the ratio of blocked to full pupil areas. This increases SNR_k for high spatial frequencies and shows that it is possible to beyond the fundamental SNR-limit.

Splitting rather than blocking

Blocking the light, as discussed above, is generally not optimal, since the formally blocked area of the pupil can be used to form a second image. Both images can be joined computationally by weighted averaging in Fourier space [7, 8] (details in supplement S3).

To improve on high spatial frequencies, where the SNR is typically low, we introduce a radial splitting of the pupil into an inner disk $\tilde{a}_{k,1}$ and outer annular ring pupil $\tilde{a}_{k,2}$, similar to the blocking scheme shown in Fig. 2b). The splitting radius correspond to a particular frequency k_s (see Fig. 3 a), which again leaves all higher spatial frequencies in the OTF unaltered (green diamonds, efficiency normalized), while the total number of photons and thus the noise is reduced (assuming an ideal detector, we are neglecting readout noise at this point).

The effects of this split-pupil approach can be summarized in an effective OTF $\tilde{h}_{k,SP}$ (see S3), which maintains uniform noise (noise-normalized, refer to [9]) equal to the FP case across all spatial frequencies and is shown in Fig. 3b) as the magenta circle markers. Comparing this to the FP-OTF (blue solid line) indicates an improvement in effective OTF strength at high spatial frequencies; albeit with a loss for intermediate frequencies (this tradeoff is described in more detail in S4). Figure 3 clearly shows that we have found a way to overcome the SNR-limit given by Fermat's principle, because we now can find a region (at high spatial frequencies) were $\tilde{h}_{k,SP} > \tilde{h}_{k,FP}$!

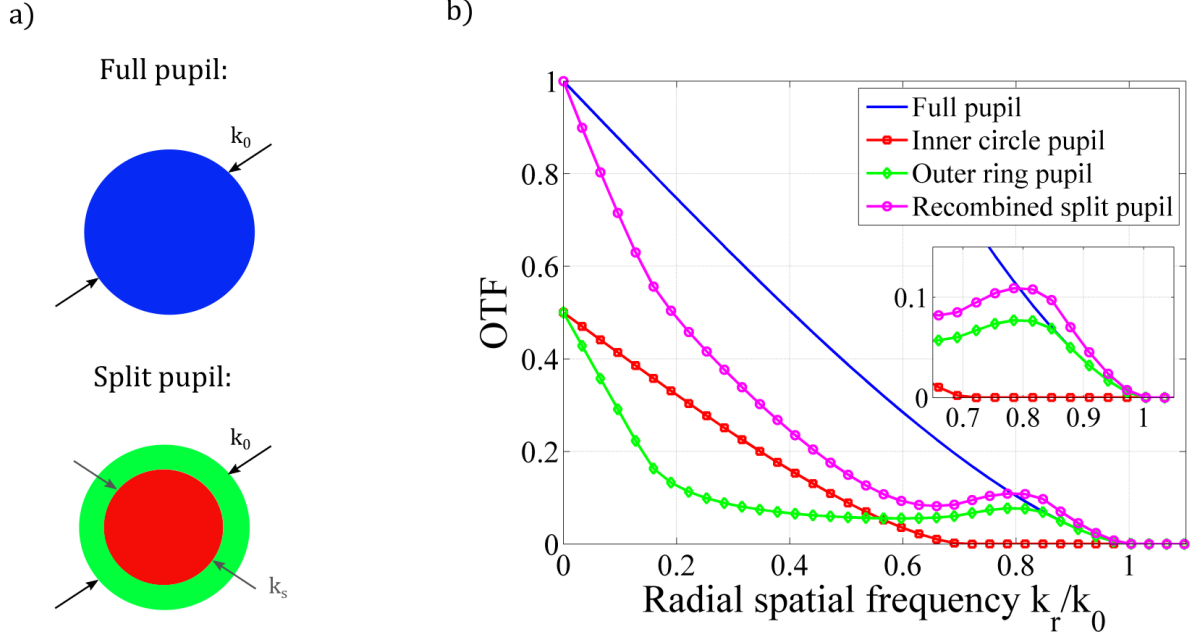


Figure 3 | Comparison between full- (FP) and split-pupil (SP) imaging in terms of transfer strength. **a)** Visualization of circular full (blue, \tilde{a}_k) and split-pupil; split into an inner circle (red, $\tilde{a}_{k,1}$) and an outer ring (green, $\tilde{a}_{k,2}$). **b)** Efficiency-normalized OTF's corresponding to FP-, the two sub-pupils and the noise-normalized recombined result. (k_r : radial spatial frequency, k_0 : system's cut-off frequency, $k_s = k_0/\sqrt{2}$ being the split frequency according to a) corresponding to the compromise described in S4. Note the improvement in OTF strength at high spatial frequencies ($\tilde{h}_{k,SP} > \tilde{h}_{k,FP}$), which indicates the circumvention of the fundamental SNR-limit, as given by Fermat's principle.

Considering the high frequencies for a given photon budget (i.e. noise level), the unmodified pupil (FP) performs sub-optimal as it would not image high spatial frequencies as well as the SP approach. The attainable SP enhancement depends on the specific splitting configuration (here $k_s = k_0/\sqrt{2}$). See supplement S4 for more details.

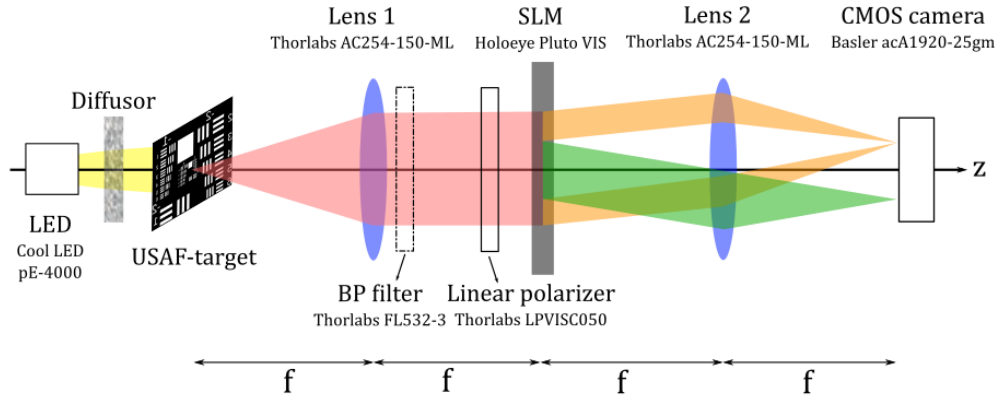
Other splitting configurations (e.g. angular-only or radial + angular splitting) and multiple splits have been numerically tested, but did not exhibit any noteworthy improvements for the general imaging case. The maximum improvement only depends on the fractional area split and not on the geometrical shape of splitting. Therefore the radial split, shown above, has the main advantage that its improvement is isotropic in k -space.

Of course people have already used several other ways to improve on SNR (e.g. temporal averaging, increase of detectors exposure time, increase illumination power, ...), but all of these methods require a certain amount of photons. Our proposed method is particularly well suited for imaging situations with a limited number of photons, e.g. fluorescent imaging or fast imaging of living specimens. We see this as the challenge our split pupil approach can overcome and were no other known technique seems to be a real alternative.

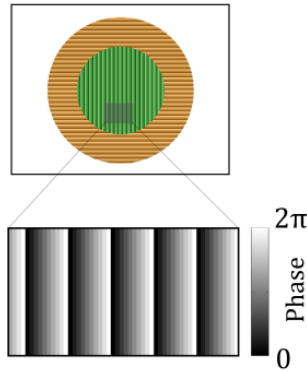
Experimental setup

We chose spatially incoherent light as generated by an LED as our light source (center wavelength $\lambda = 525$ nm). A thin (diffusing) plastic plate was put in front of a USAF 1951-target (Thorlabs Inc., NJ), ensuring its homogeneous maximally incoherent illumination. Fig. 4 shows the $4f$ -imaging system as previously introduced in Fig. 1, which is easily accessible through a side port of the microscope body (nowadays provided by all manufactures).

a)



b)



c)

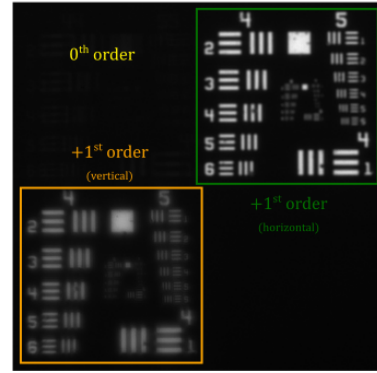


Figure 4 | Depiction of the experimental setup, the splitting mechanism and the resulting sub-images. a) Incoherent $4f$ -imaging system including an SLM placed into the pupil plane (c.f. Fig. 1 a). Note that the green beam is actually directed orthogonal to the plane of the figure. b) The pupil was split by displaying two orthogonally oriented blazed phase gratings, resulting in the spatially separate acquisition of both sub-images on a single camera. c) Captured camera image with both sub-images. The frame color refers to the color of the respective sub-pupil shown in b).

A spatial light modulator (SLM) placed in the pupil plane enabled the programmable simultaneous imaging via sub-pupils. The reflective SLM (Holoeye Pluto VIS, Germany) is depicted in Fig. 4 a) as a transmission device, to keep it conceptually simple. The phase distribution displayed on the SLM for a radial splitting configuration is schematically shown in Fig. 4b). Two linearly blazed phase gratings direct the light onto separate areas on the detector. These gratings were vertically (inner circle pupil $\tilde{a}_{k,1}$, green) and horizontally (outer ring pupil $\tilde{a}_{k,2}$, orange) aligned, causing their respective diffraction orders to *not* overlap. These orthogonal oriented directions also avoid possible influences of residual zero, negative or higher diffraction orders.

Because this particular splitting mechanism is based on diffraction, it is required that the light impinging on the SLM is monochromatic, hence a narrow bandpass (BP)-filter (Thorlabs, NJ, FWHM 532 ± 3 nm) was used. The linear polarization filter (Thorlabs, NJ) was required due to the polarization-requirements of the SLM. Details on how to build a more efficient system that can also be used for broadband imaging, as well as the apparent tradeoff between field-of-view (FoV) and SNR-improvement is discussed later.

The modification of the optical system's pupil yields two sub-images (see Fig. 4 c, note the annotations indicating the different position of the respective diffraction orders), which we captured using a CMOS-camera (Basler acA1920-25gm, Germany). The images were cropped, computationally registered and recombined by weighted averaging in Fourier-space. For this proof-of-concept experiment, the full-pupil images have been obtained by imaging via a clear pupil of the same size, here realized by a single vertically aligned blazed grating covering the whole pupil diameter.

Experimental results

The recombination of the sub-pupil images by weighted averaging in Fourier-space requires the knowledge of the individual sub-OTFs, corresponding to each of the sup-pupils (see supplement S4) [9]. These OTFs were computed using [10] and validated against experimentally measured PSFs (see S5).

Both images (FP and SP) are compared in figure 5. The three boxes (orange, cyan & magenta) represent three different spatial frequency line patterns in the object (given in line-pairs, lp per mm):

- **Orange**, $k_{low} = 20.1 \text{ lp/mm} = 0.45 k_0$: SP result has reduced contrast \rightarrow *worse* optical transfer
- **Yellow**, $k_{high} = 35.9 \text{ lp/mm} = 0.79 k_0$: SP result has higher contrast \rightarrow *better* optical transfer
- **Magenta**, $k_0 = 40.3 \text{ lp/mm} = 0.89 k_0$: *Increased* effective resolution limit for SP-result.

The maximum transferrable frequency in the given system was $k_0 \approx 45.3 \text{ lp/mm}$, as given by the first line structure which could not be visually resolved (marked by small yellow arrow; it corresponds to the diffraction limit given by $\Delta x \approx 22 \mu\text{m}$).

As discussed before, the SP-approach yields an increased effective resolution limit. For the imaging of the USAF-1951 line patterns, we thus expect higher modulation strength at line patterns corresponding to high frequencies.

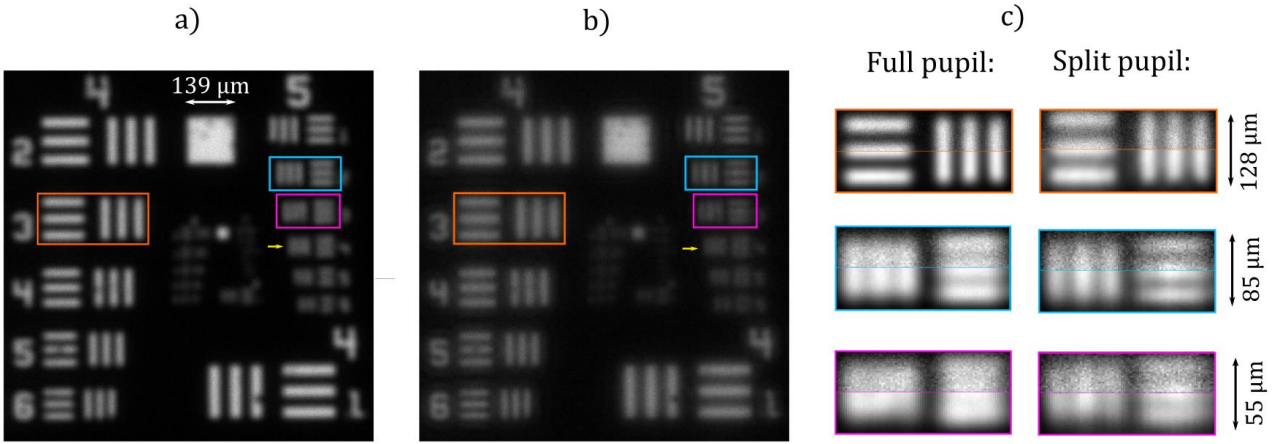


Figure 5 | Experimental full- and split-pupil comparison of an USAF-1951 target. **a)** Single image FP result, boxes (orange, cyan & magenta) correspond to three different spatial frequencies ($k_1 = 0.45 k_0$, $k_2 = 0.79 k_0$ & $k_3 = 0.89 k_0$). **b)** Single image SP result, showing an overall reduced brightness, discussed in S7. **c)** Visual comparison between the three line pattern groups, where each line group has been normalized to its respective maximum intensity value (top: single image; bottom: average of 100 images to remove noise). The difference in modulation depth can be directly compared to the difference in optical transfer strength shown in Fig. 3. See Fig. 6 for corresponding profile line plots for k_1 & k_2 . In the case of k_3 (magenta frame) it can be seen that the SP-method increases the effective resolution limit of the system, hence breaks the SNR-limit. The yellow arrow indicates the diffraction limit given by $k_0 \approx 45.3 \text{ lp/mm}$, which corresponds in real space to $\Delta x \approx 22 \mu\text{m}$ (see S5).

Figure 5 c) shows the different line groups in more detail. In each sub-frame the top shows the respective line pattern as a single image and on the bottom as an average of 100 images, to reduce noise. It can be clearly seen, that the SP-result shows a reduced modulation depth for k_1 , but outperforms the FP-result in case of higher frequencies k_2 & k_3 . This already indicates that we have overcome the fundamental SNR-limit, using a method that only requires a single acquisition process.

Since the recombination takes place in Fourier-space, an evaluation of the performance of FP- to SP-result can be done by defining an improvement factor with respect to SNR ($IF_{k_r, SNR}$):

$$IF_{k_r, SNR} = \frac{SNR_{k_r, SP}}{SNR_{k_r, FP}} - 1 \quad (6)$$

With $SNR_{k_r,FP}$ & $SNR_{k_r,SP}$ being the signal-to-noise ratios of the full- and split-pupil result respectively. A positive $IF_{k_r,SNR}$ indicates an improvement of the SP- compared to the FP-result.

This is depicted in Fig. 6a), for the experimental data, as a 2D-plot (top) and as a radial mean (bottom, expectancy and standard deviation calculated using 100 sequentially acquired images). Both graphs confirm that an SNR-improvement occurs at high spatial frequencies and can be directly compared to the theoretical prediction given in S4 (root-mean-square-error RMSE ≈ 0.15).

To quantitatively evaluate the image data in real space, the expectancy and standard deviation (over 100 individual images) of the two different line patterns have been plotted in Fig. 6 b) & c) (two frequencies k_1 & k_2 ; horizontal orientation; vertical results shown in S6 confirm isotropy of the proposed method).

The top row depicts the expectancy, whereas the bottom shows the standard deviation for the horizontal oriented line patterns.

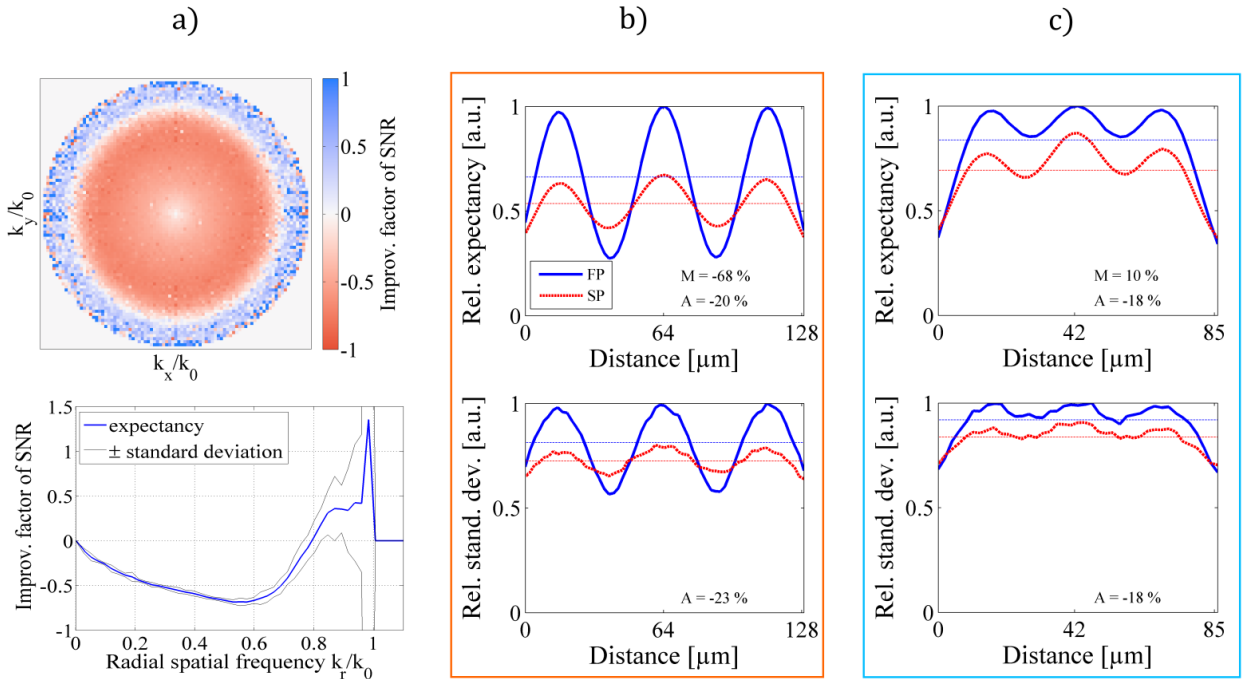


Figure 6 | Experimentally achieved improvement in Fourier and real space. a) 2D-plot (top) and radial mean plot (bottom) of $IF_{k_r,SNR}$ in Fourier space. b) Profile plot of horizontal oriented line pattern with ($k_1 = 0.45 k_0$, orange box in Fig. 5) and c) ($k_2 = 0.79 k_0$, cyan box). The expectancy (top) and standard deviation (bottom) of the FP- (blue, thick line) and SP-image (red, thick line) has been calculated using 100 acquired images. The dashed horizontal lines correspond to the average value calculated over the respective window size. The relative differences between the average value A and the modulation depth M (c.f. text) are given as an inset. Note that the line plots for the vertically aligned line groups are shown in S6 confirming the isotropic improvement of the proposed method.

The relative change in modulation depth M (modulation amplitude divided by average) is determined as:

$$M = \frac{M_{SP} - M_{FP}}{M_{FP}} \quad (7)$$

and stated in each figure panel. Correspondingly the relative change in average intensity computed over the respected box is also stated.

The data displayed in the orange box shows that the SP-method reduced the modulation depth for k_1 . This is seen in Fig. 5b) as an enhanced blur in the orange box. Note that the overall number of photons is approximately equal in both FP- and SP-images. The 20 % reduced average can be explained by more energy being shifted outside the box as detailed in S7.

The split pupil is seen to perform superior to the full pupil for high spatial frequencies (cyan & magenta boxes). For the cyan box, the modulation depth is enhanced by 10 % and the average value is reduced by 18 %, along with a reduced standard deviation (blue curves Fig. 6c). High spatial frequencies were transferred with greater modulation depth and lower image noise. As especially visible in the magenta box (Fig. 5c), where the modulation is only be seen for the split pupil approach, the SNR-limit has been overcome.

The reduced contrast at medium spatial frequencies (Fig. 6, orange box) is not a practical problem as long as it does not fall under the noise limit. A deconvolution, as achieved for example by Wiener filtering [11], can almost fully restore this contrast. A comparison of both results (FP and SP) is shown in Fig. 7 a) and b):

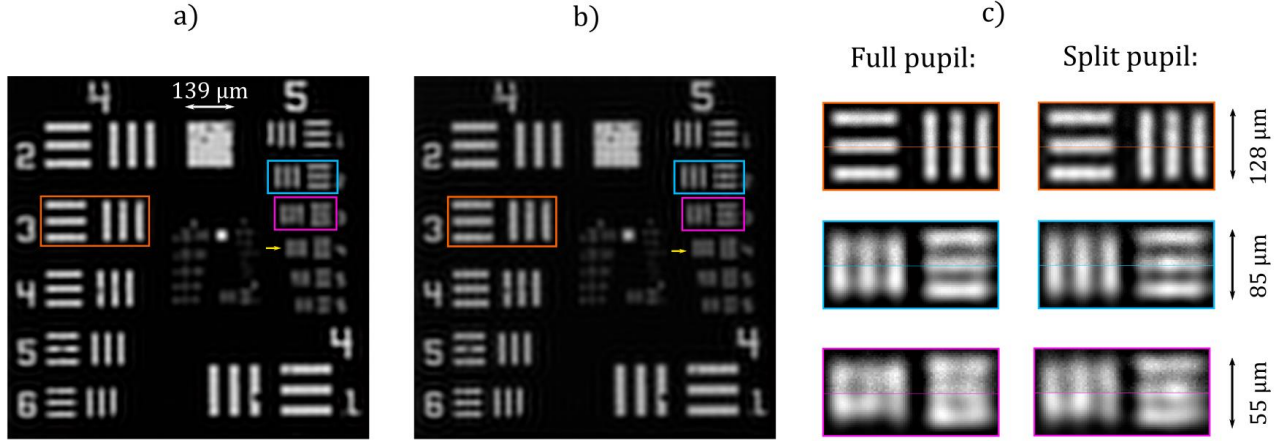


Figure 7 | Experimental full- and split-pupil comparison of an USAF-1951 target after Wiener filtering. a) and b) show the result of a Wiener deconvolution using a regularization parameter of $\tau = 0.01$ [11]. The colored boxes (orange, cyan & magenta) represent different spatial frequencies ($k_1 = 0.45 k_0$, $k_2 = 0.79 k_0$ & $k_3 = 0.89 k_0$), as already introduced in Fig. 5. The yellow arrow indicates the diffraction limit of the used optical system, given as $k_0 \approx 45.3$ lp/mm. c) shows the individual boxes in more detail and provides a direct comparison between FP and SP result (each sub-frame is normalized to its respective maximum intensity value; top: single image; bottom: average over 100 images to reduce noise). It can be clearly seen that after deconvolution the results for the low frequency (orange box) are quite similar, whereas at high frequencies (cyan & magenta) the SP result still maintains a better contrast.

Similar to figure 5, the colored boxes represent different spatial frequencies. The corresponding line patterns are shown in more detail in c). Details on the deconvolution parameters are described in the methods part. Note that after deconvolution the visibility of the high frequency line patterns (cyan & magenta) is still maintained for the SP-method, whereas mid frequencies (orange) only suffer from slightly enhanced noise. After deconvolution, the SP approach can be regarded as a superior imaging modality in a more general sense, especially when dealing with a limited number of photons.

Discussion

The method of splitting the pupil of an incoherent imaging system and computationally combining the measured sub-pupil images has been experimentally shown to outperform the classical imaging via an unobstructed pupil. Since for many imaging tasks a certain minimum SNR plays a major role, the split pupil approach has a wide range of applications in fields ranging from metrology to bio-imaging. Especially in the field of metrology an imaging task can be sometimes defined very specifically (e.g. the identification of manufacturing defects), in which case tailored pupil splits may lead to very large relative SNR improvements, e.g. allowing a very significant reduction of exposure time.

One may argue that drawing a single uniform line to represent the noise level in Fourier space is somewhat misrepresenting the fact that photon noise is localized in real space. However, the general argument of improved SNR for split-pupil imaging still holds albeit for a smaller region around the feature of interest.

Of course, modification of the pupil of an imaging system, to realize a performance improvement, has already been realized before. But none of these techniques specifically address the issue of breaking the SNR-limit of conventional imaging by pupil splitting and subsequent recombination. Usually their development have different purposes, like realizing imaging in the X- or gamma-ray regime in the case of coded aperture imaging [12, 13], reduction of side lobes of the airy disk using apodization [14] or closing down of the pupil to avoid aberrations at the edge of the pupil, as is often done by optical designers.

Currently available techniques differ in two main aspects from our proposed method:

- 1.) In our splitting approach we (theoretically) do not lose any photons, which is the reason why we can compare our approach to conventional (full pupil) imaging in the first place. All aforementioned already existing methods do **not** make use of all the photons and therefore could not be compared against a FP system, in terms of efficiency.
- 2.) None of the previous methods try to overcome the fundamental SNR-limit at high spatial frequencies. They all stay within the boundaries of the conventional FP-OTF. Our method goes beyond that and shows that it is possible to get more information out of the already captured light, through pupil splitting.

Manipulating the pupil of an imaging system, to specifically improve on resolution, has already been done before [15, 16] and is not the intention of our work. Our goal is to show a novel way how to overcome the SNR-limit in incoherent imaging. We only have chosen to represent the improvement in SNR as an increase of the effective resolution limit, which by no means is comparable to already established super-resolution techniques. Using an objective with a higher numerical aperture would already beat the SP approach in terms of resolution, but also would make use of a larger number of photons. This violates the restriction of photon limitation that we have set out in the beginning. Therefore the comparison between high- NA objective and our proposed SP-imaging is unfair.

Additionally at some point an increase in NA is not possible anymore. Here our method can still achieve an improvement in terms of SNR, which enables us to obtain information that in conventional imaging would have already been lost. This is especially true in the case of very photon-limited imaging scenarios. Therefore our proposed approach is at the forefront of technology and might be crucial for future developments of fast and light-sensitive imaging systems.

In practice, an SLM-based splitting scheme, as presented here may be far from optimal, due to its limitations to monochromatic polarized light and additional losses in the reflectivity. However, this could be remedied by manufacturing dedicated mirror-based split pupils which are more efficient and can be used in the case of imaging with polychromatic light. Another approach would be to realize the split pupil imaging by making use of meta-materials, e.g meta-gratings as proposed in [17].

Of course the achievable improving on SNR comes at the cost of requiring double the field-of-view (FoV), compared to a conventional imaging system. In principle this tradeoff between space-bandwidth product (SBP) and SNR enhancement at high spatial frequencies is also present when using an objective with a larger NA . Fortunately nowadays the manufacturing of focal-plane array detectors in the visible range has become a state-of-the-art technique, so that using two separate cameras has become quite cheap. In comparison, it is much more difficult to design a high NA objective with double the FoV. Hence our proposed method seems to be a very useful technique to improve on SNR for high NA imaging.

As supplement S8 shows, the effective PSF of our system is axially elongated, hence exhibits a longer depth-of-field (DoF), as it is often wanted in extended-depth-of-field (EDoF) imaging [18, 19]. Our simulation shows that we can improve on the axial elongation by a factor of two (when splitting into two equal area sub-pupils, see S8), which might be useful for fast-volumetric imaging [20]. Furthermore it can

be seen that the SNR-enhancement at high spatial frequencies scales with the numerical aperture, hence our SP-approach seems to be a valuable tool for high- NA imaging scenarios.

Due to the required splitting we obtain *two* individual sub-images, which increases readout noise by a factor of *two*. Modern cameras exhibit a readout noise level of about $5 - 10 e^-$ RMS (root-mean-square) at a readout rate of $20 - 500$ kHz [21]. In our case the readout rate was in the order of 1 kHz, hence we would deal with an increase of readout noise (due to the splitting) of $\approx 1 e^-$. Even in the photon-limited regime, the generated number of photo-electrons usually is $\gg 1$. Therefore we can safely neglect readout noise in our theoretical treatment.

Conclusion

We demonstrated imaging with better SNR compared to classical full pupil based images, hence split pupil imaging can be “better than a lens”. The enhancement is restricted to high spatial frequencies and becomes very significant at regions, which are very close to the cut-off frequency of the optical system. This gives the split pupil imaging approach a unique advantage over other techniques and goes beyond the SNR-limit given by Fermat’s principle in a novel and fundamentally new way. The strength of our proposed method can be fully exploited in the case of very photon-limited high NA imaging, where no competing technique exists so far.

Methods

The components of our optical bench setup (Fig. 4) are mentioned in the figure. Alignment was achieved by removing the USAF-1951 sample and diffusor and centring the illumination and back reflections.

To achieve exact pupil positioning, the SLM was first visually centred with the illumination beam. Then a disc containing a blazed grating was displayed and computationally moved until optimum image quality was achieved for all features and feature orientations of the USAF-1951 target. Due to the simplicity of the optical setup (two lenses and a single SLM) the alignment seems not to be a critical issue.

The SLM has been used in an extended desktop mode and all SLM masks were created using *Octave*. The maximum 2π retardance-value of the grating has been determined manually by maximizing the diffraction efficiency of the first order.

The exposure time for any measurement (USAF-1951 target or PSF-measurement) was adjusted as to prevent detector saturation. For the comparison of the experimental data, both (FP & SP) images were acquired with an identical exposure time of 10 ms. Note that the issue of detector saturation is not critical, since we are splitting the light. Hence in the case saturation occurs using our method, it will definitely also occur in convention FP imaging. Therefore our proposed approach is more immune towards detector saturation.

Sub-images were cropped manually and residual shift-correction has been applied using the *findshift*-routine of the *dipimage* toolbox [22] in *Matlab* (Mathworks, MA). Also the discrete Fourier-transform has been used from this package.

In the weighted averaging reconstruction we have used PSFs calculated using [10]. To verify their validity we have also obtained experimental PSFs. Comparison between both can be seen in supplement S5. Note that we haven’t used any kind of prior and that every reconstruction algorithm comes with the downside of artifacts. We have found empirically that these are rather small for SP-imaging and therefore are neglected in our discussion.

In case that both sub-images undergo different kind of aberrations, we can still reconstruct an ideal SNR-result provided we have access to measured PSFs. In any real application scenario it would be crucial to minimize aberrations of the optical system, but again, this is true for all imaging system in general.

For deconvolution we have used wiener filtering [10] with a regularisation parameter of $\tau = 0.01$ for both datasets (FP & SP). Note that τ has been found empirically for both imaging modalities individually.

The expectancy values shown in Fig. 6 have been obtained by calculating the average of 100 sequentially acquired images. Due to the (weak) *law of large numbers* [4], the average is an estimate for the expectancy, given a high enough number of averaged images (100 images seems to be enough, no visible noise contribution in Fig. 5 & 7).

References

- [1] Michael Sean Mahoney, *The Mathematical Career of Pierre de Fermat, 1601-1665*, 2nd edition (Princeton University Press, 1994), p. 401
- [2] Novotny, L., & Hecht, B. (2006). *Principles of Nano-Optics*. Cambridge: Cambridge University Press. doi:10.1017/CBO9780511813535
- [3] Goodman, Joseph W., *Introduction to Fourier Optics*, New York: McGraw-Hill, 1996.
- [4] Ernst Abbe, *Beiträge zur Theorie des Mikroskops und der mikroskopischen Wahrnehmung*. In: *Archiv für mikroskopische Anatomie*. Band 9, Nr. 1, Dezember 1873, doi:10.1007/BF02956173, urn:nbn:de:hebis:30-1123587.
- [5] Bronstein I. N., Semendjajew K. A., *Taschenbuch der Mathematik*, 5. Auflage, B. G. Teubner Verlagsgesellschaft, Leipzig.
- [6] Robert L. Lucke, *Fourier-space properties of photon-limited noise in focal plane array data, calculated with the discrete Fourier transform*, J. Opt. Soc. Am. A 18, 777-790 (2001).
- [7] Gustafsson, M. G. L. (2000): *Surpassing the lateral resolution limit by a factor of two using structured illumination microscopy*; Journal of Microscopy, 198: 82-87. doi: 10.1046/j.1365-2818.2000.00710.x.
- [8] Heintzmann R., et al., *Resolution enhancement by subtraction of confocal signals taken at different pinhole sizes*, *Micron*, 34(6-7), 293 - 300. DOI: 10.1016/S0968-4328(03)00054-4
- [9] Wicker Kai: *Increasing resolution and light efficiency in fluorescence microscopy*, dissertation, Kings College London. October 2010
- [10] Richards B. and Wolf E., *Electromagnetic diffraction in optical systems II. Structure of the image field in an aplanatic system"*, Proc. R. Soc. London A, vol. 253, no. 1274, 1959.
- [11] Wiener, Norbert, et al. *Extrapolation, interpolation, and smoothing of stationary time series: with engineering applications*. (1949). New York: Wiley. ISBN 0-262-73005-7.
- [12] Ables, J. G., *Fourier transform photography: a new method for X-ray astronomy*. Publications of the Astronomical Society of Australia 1.4 (1968): 172-173.
- [13] Dicke, R. H., *Scatter-hole cameras for x-rays and gamma rays.*" The astrophysical journal 153 (1968): L101.
- [14] MacDonald, J. A., *Apodization and frequency response with incoherent light. Proceedings of the Physical Society* 72.5 (1958): 749.
- [15] Barakat, Richard., *Application of apodization to increase two-point resolution by the Sparrow criterion. I. Coherent illumination. JOSA* 52.3 (1962): 276-283.
- [16] Barakat, Richard, and Elgie Levin., *Application of apodization to increase two-point resolution by the Sparrow criterion. II. Incoherent illumination. JOSA* 53.2 (1963): 274-282.
- [17] Khorasaninejad, Mohammadreza, and Federico Capasso. Broadband multifunctional efficient meta-gratings based on dielectric waveguide phase shifters. *Nano letters* 15.10 (2015): 6709-6715.
- [18] Indebetouw, Guy, and Hanxian Bai. *Imaging with Fresnel zone pupil masks: extended depth of field. Applied Optics* 23.23 (1984): 4299-4302.
- [19] Dowski, Edward R., and W. Thomas Cathey. *Extended depth of field through wave-front coding. Applied optics* 34.11 (1995): 1859-1866.
- [20] Tomer, Raju, et al. *SPED light sheet microscopy: fast mapping of biological system structure and function. Cell* 163.7 (2015): 1796-1806.

[21] van Vliet, Lucas J., Damir Sudar, and Ian T. Young. *Digital Fluorescence Imaging Using Cooled CCD Array Cameras invisible*. *JE Celis (eds); Cell Biol. Second Edition* 3 (1998): 109-120.

[22] Luengo Hendriks CL, Van Vliet LJ, Rieger B, van Kempen GMP, and van Ginkel M. Dipimage: a scientific image processing toolbox for matlab. Quantitative Imaging Group, Faculty of Applied Sciences, Delft University of Technology, Delft, The Netherlands, 1999.

Acknowledgements

We would like to thank Colin J. R. Sheppard, Polina Feldmann, Christian Karras and Walter Müller for interesting and fruitful discussions concerning the basic idea, theoretical implications and the experimental realization. The authors acknowledge infrastructural funding by *Inphodeg*.

Author contributions

R.H. conceived the initial idea. J.B. worked on the theoretical details, the numerical investigation and performed the experiment. R.F. helped in the theoretical understanding and experimental realization.

Additional information

Correspondence and requests for materials should be addressed to R.H.

Competing financial interests

The authors declare no competing financial interests.

Supplementary material:

S1 The autocorrelation operation in a graphical representation:

As stated in the main text, the autocorrelation operation given in equation (2) can be visualized as quantifying the amount of difference vectors, which connect non-zero points of a given pupil. For a given spatial frequency vector \vec{k} , this results in the blue area shown in figure S1.

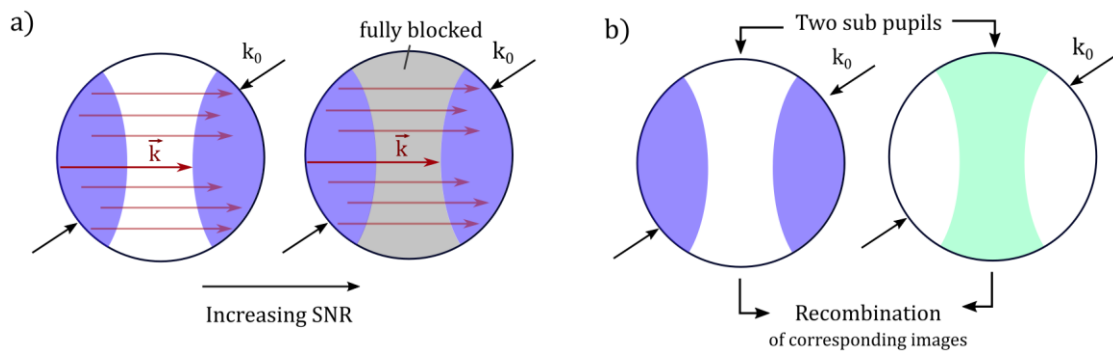


Figure S1 | Graphical representation of the autocorrelation operation and the effects of blocking or splitting the pupil. a) The blue area corresponds to all points within the pupil that can be connected by a spatial frequency \vec{k} (red arrows). *Left:* Full pupil, hence there exist a region (white area) which does not contribute to the incoherent optical transfer function at \vec{k} . *Right:* Blocking of this part (now grey area) does not affect any of the connecting difference frequency vectors but reduces the total number of photons and thus reduces the noise. Therefore the SNR at this \vec{k} is improved. **b)** Instead of blocking a part of the pupil, this area can be used to simultaneously record a separate image. Both sub-images are then subsequently recombined computationally, yielding an improved high frequency SNR result.

The number of difference vectors (red arrows) yields the OTF-strength for a particular frequency \vec{k} . The area on which connecting difference vectors of a given length and orientation reside is equal for both panels in Fig. S1a). Hence both pupils yield equal transfer strength in the incoherent OTF. Yet on the right side of panel a, the part of the pupil, which does not contribute to the

transfer at this spatial frequency is completely blocked which reduces the total number of detected photons in proportion to that area. Less photons reduce the image variance (see S2) and therefore increases the SNR at this particular spatial frequency \vec{k} .

As shown in Fig. S1 b) a better approach is the computational recombination of sub-images obtained via both sub-pupils. Because each of them carries different spatial frequencies the recombination yields an overall better transfer of object information than each individual sub-image for itself.

Altogether this shows that the proposed method has its strength in enhancing mostly a small region of frequencies close to the cut-off frequency of the system.

S2 Properties of image data including by photon-limited noise:

We assume photon-limited noise in which the signal (I_r) of each pixel r follows a Poisson-distribution [4] with an expectancy μ_r (index r referring to the respective pixel number):

$$\mathcal{P}\{I_r|\mu_r\} = \frac{\mu_r^{I_r} e^{-\mu_r}}{I_r!} \quad (S1)$$

In a Poisson-distribution variance σ_r^2 is equal to the expectancy μ_r :

$$\langle I_r \rangle = \mu_r \quad (S2)$$

$$\text{Var}\{I_r\} = \sigma_r^2 = \mu_r \quad (S3)$$

The Poisson-distribution applies to the measurements performed in real space, where the variance is signal dependent (index r). Since we want judge the imaging performance in Fourier space, we need to describe the noise in k -space. To do this we calculate the variance of Fourier-transformed ($\mathcal{F}\{.\}$) data [5]:

$$\text{Var}\{\tilde{I}_k\} = \text{Var}\{\mathcal{F}\{I_r\}\} \approx \text{Var}\{\sum_r I_r e^{-ikr}\} \quad (S4)$$

with the following definition of the variance of a complex quantity $X \in \mathbb{C}$:

$$\text{Var}\{X\} := \text{Var}\{\text{Re}\{X\}\} + \text{Var}\{\text{Im}\{X\}\} \quad (S5)$$

Note that the usual pre-factors in front of the Fourier-sum have been omitted. Since the I_r are statistically independent, equation (S4) can be re-written as:

$$\text{Var}\{\tilde{I}_k\} \approx \sum_r \text{Var}\{I_r e^{-ikr}\} \quad (S6)$$

Knowing that the variance of a random variable X obeys the following property [4]:

$$\text{Var}\{aX\} = a a^* \text{Var}\{X\} = |a|^2 \text{Var}\{X\} \quad (S7)$$

with a being a complex constant $a \in \mathbb{C}$, we can express equation (S6) as:

$$\text{Var}\{\tilde{I}_k\} \approx \sum_r |e^{-ikr}|^2 \text{Var}\{I_r\} = \sum_r \text{Var}\{I_r\} = \sum_r \mu_r \quad (S8)$$

This equation shows that the variance in Fourier-space is independent of k and that its magnitude is proportional to the total number of expected photons.

With this we can define the SNR in Fourier-space as:

$$\text{SNR}_k = \frac{|\langle \tilde{I}_k \rangle|}{\sqrt{\text{Var}\{\tilde{I}_k\}}} = \frac{|\langle \tilde{I}_k \rangle|}{\sqrt{\sum_r \mu_r}} \quad (S9)$$

Note the abs. value in the numerator, which has been included to obtain a real-valued property.

Equation (S9) indicates that in Fourier-space the SNR can be increased by reducing the total number of photons as long as the transfer stays constant.

S3 Recombination of the split image data yielding an effective (noise-normalized) OTF:

The optical system's pupil is split into M -different sub-pupils $\tilde{a}_{k,m}$, with $m \in [1, M]$, (e.g. $M = 2$). This yields M -different sub-images $\tilde{I}_{k,m}$ corresponding to the individual sub-OTFs $\tilde{h}_{k,m}$:

$$\tilde{I}_{k,m} = \tilde{S}_k \tilde{h}_{k,m} \quad (\text{S10})$$

By splitting the pupil, the variance is as well separated [2]:

$$\tilde{\sigma}_m^2 = \text{Var}\{\tilde{I}_{k,m}\} \quad (\text{S11})$$

$$\sum_m^M \tilde{\sigma}_m^2 = \tilde{\sigma}^2 = 1 \quad (\text{noise-normalized}) \quad (\text{S12})$$

The different sub-images get recombined by performing weighted-averaging in Fourier-space [6]:

$$\tilde{I}_{k,wa} = 1 / \sum_l^M \tilde{w}_{k,l} \sum_m^M \tilde{w}_{k,m} \tilde{I}_{k,m} \quad (\text{S13})$$

With the frequency-dependent weights $\tilde{w}_{m,k}$ differing between the individual sub-images. Note that the noise in Fourier-space is correlated. This correlation has been neglected in our reconstruction algorithm. An inclusion might only lead to minor improvements. The weighted average shown here is an incoherent addition and makes no use of any phase relation between the sub-images, as well as of any kind of priors. For a discussion on reconstruction artifacts refer to the methods part.

This leads to a variance of the weighted averaged result:

$$\tilde{\sigma}_{k,wa}^2 = \text{Var}\{\tilde{I}_{k,wa}\} = 1 / \left[\sum_l^M \tilde{w}_{k,l} \right]^2 \sum_m^M [\tilde{w}_{k,m} \tilde{\sigma}_m]^2 \quad (\text{S14})$$

The corresponding weights are found by maximizing the $SNR_{k,wa}$:

$$\begin{aligned} SNR_{k,wa} &= \frac{|\tilde{I}_{k,wa}|}{\sqrt{\text{Var}\{\tilde{I}_{k,wa}\}}} = \frac{|\tilde{I}_{k,wa}|}{\sqrt{\tilde{\sigma}_{k,wa}^2}} \\ &= \frac{|\tilde{S}_k| \sum_m^M \tilde{w}_{k,m} \tilde{h}_{k,m}}{\sqrt{\sum_{m'}^M [\tilde{w}_{k,m'} \tilde{\sigma}_{m'}]^2}} \end{aligned} \quad (\text{S15})$$

To keep it simple, it was assumed that the weights and the sub-OTFS are real-valued and positive:

$$\tilde{w}_{k,m}, \tilde{h}_{k,m} \in \mathbb{R} \quad \wedge \quad \tilde{w}_{k,m}, \tilde{h}_{k,m} \geq 0 \quad (\text{S16})$$

To optimize SNR, we need to look for the condition: $\partial SNR_{k,wa} / \partial \tilde{w}_{k,l} = 0$:

$$\frac{\partial SNR_{k,wa}}{\partial \tilde{w}_{k,l}} = |\tilde{S}_k| \frac{\tilde{h}_{k,l} \sum_m^M [\tilde{w}_{k,m} \tilde{\sigma}_m]^2 - \tilde{w}_{k,l} \tilde{\sigma}_l^2 \sum_{m'}^M \tilde{w}_{k,m'} \tilde{h}_{k,m'}}{\sqrt{\sum_{m''}^M [\tilde{w}_{k,m''} \tilde{\sigma}_{m''}]^2}^{3/2}} = 0 \quad (\text{S17})$$

This yields:

$$\tilde{h}_{k,l} \sum_m^M [\tilde{w}_{k,m} \tilde{\sigma}_m]^2 = \tilde{w}_{k,l} \tilde{\sigma}_l^2 \sum_{m'}^M \tilde{w}_{k,m'} \tilde{h}_{k,m'} \quad (\text{S18})$$

When both terms in front of the two sums equal, also the sums themselves will vanish:

$$\tilde{h}_{k,l} \sum_m^M [\tilde{w}_{k,m} \tilde{\sigma}_m]^2 = \tilde{h}_{k,l} \sum_{m'}^M [\tilde{w}_{k,m'} \tilde{\sigma}_{m'}]^2 \quad (S19)$$

Which corresponds to the following weights:

$$\tilde{w}_{k,m} = \frac{\tilde{h}_{k,m}}{\tilde{\sigma}_m^2} \quad (S20)$$

In contrast to unprocessed images, the obtained variance $\tilde{\sigma}_{k,wa}^2$ now depends on k (c.f. eq. S14). A direct comparison to the FP-image would be unfair due to different noise characteristics. Hence as a final step, $\tilde{I}_{k,wa}$ needs to be noise-normalized. This is achieved by a division by its standard deviation $\tilde{\sigma}_{k,wa}$ [8], resulting in:

$$\tilde{I}_{k,SP} = \frac{\tilde{I}_{k,wa}}{\tilde{\sigma}_{k,wa}} = \frac{\sum_m^M \frac{\tilde{h}_{k,m}^2}{\tilde{\sigma}_m^2} \tilde{S}_k}{\sqrt{\sum_l^M \frac{\tilde{h}_{k,l}^2}{\tilde{\sigma}_l^2}}} = \sqrt{\sum_m^M \frac{\tilde{h}_{k,m}^2}{\tilde{\sigma}_m^2}} \tilde{S}_k \quad (S21)$$

This yields a normalized variance, which does not depend on k :

$$\text{Var}\{\tilde{I}_{k,SP}\} = \text{Var}\left\{\frac{\tilde{I}_{k,wa}}{\tilde{\sigma}_{k,wa}}\right\} = \frac{\text{Var}\{\tilde{I}_{k,wa}\}}{\tilde{\sigma}_{k,wa}^2} = 1 \quad (S22)$$

Altogether the recombination and noise-normalization can be summarized into an effective OTF $\tilde{h}_{k,SP}$, which mimics the basic imaging equation (1) in Fourier space:

$$\tilde{I}_{k,SP} = \tilde{h}_{k,SP} \tilde{S}_k \quad (S23)$$

with:

$$\tilde{h}_{k,SP} = \sqrt{\sum_m^M \frac{\tilde{h}_{k,m}^2}{\tilde{\sigma}_m^2}} \quad (S24)$$

The effective OTF of the split pupil imaging approach is equal to the square-root of the sum over the squared sub-OTF's $\tilde{h}_{k,m}$ scaled by their respective sub-image variance $\tilde{\sigma}_m^2$.

S4 Definition of the improvement factor, it's maximum value and the required tradeoff:

The enhancement of the proposed split-pupil imaging method can be investigated by introducing the improvement factor IF_{k_r} , defined as:

$$IF_{k_r} = \frac{|\tilde{h}_{k_r,SP}|}{|\tilde{h}_{k_r,FP}|} - 1 \quad (S25)$$

A positive value of IF_{k_r} indicates some improvement with respect to the FP-result. In the case of a radial split, as done in this work, the dependency of IF_{k_r} depends on the splitting radius k_s . This dependency is shown in figure S4.

Increasing the inner circle pupil radius leads to a stronger maximum improvement IF_{max} , while the losses at the mid-frequencies increase as well.

In Fig. 3 we observe that the maximum improvement of the split-pupil result occurs at those frequencies at which the outer ring OTF is equal to the FP-OTF. This means that from a frequency k_r' onwards, the effective split-pupil OTF can be written as:

$$\tilde{h}_{k_r \geq k_r', SP} = \sqrt{0 + \frac{\tilde{h}_{k_r \geq k_r', FP}^2}{\tilde{\sigma}_2^2}} = \frac{\tilde{h}_{k_r \geq k_r', FP}}{\tilde{\sigma}_2} \quad (S26)$$

Therefore we define the maximum improvement factor as follows:

$$IF_{max} = IF_{k_r \geq k_r'} = \frac{\tilde{h}_{k_r \geq k_r', SP}}{\tilde{h}_{k_r \geq k_r', FP}} - 1 = \frac{\tilde{h}_{k_r \geq k_r', FP}}{\tilde{h}_{k_r \geq k_r', FP}} - 1 = \frac{1}{\tilde{\sigma}_2} - 1 \quad (S27)$$

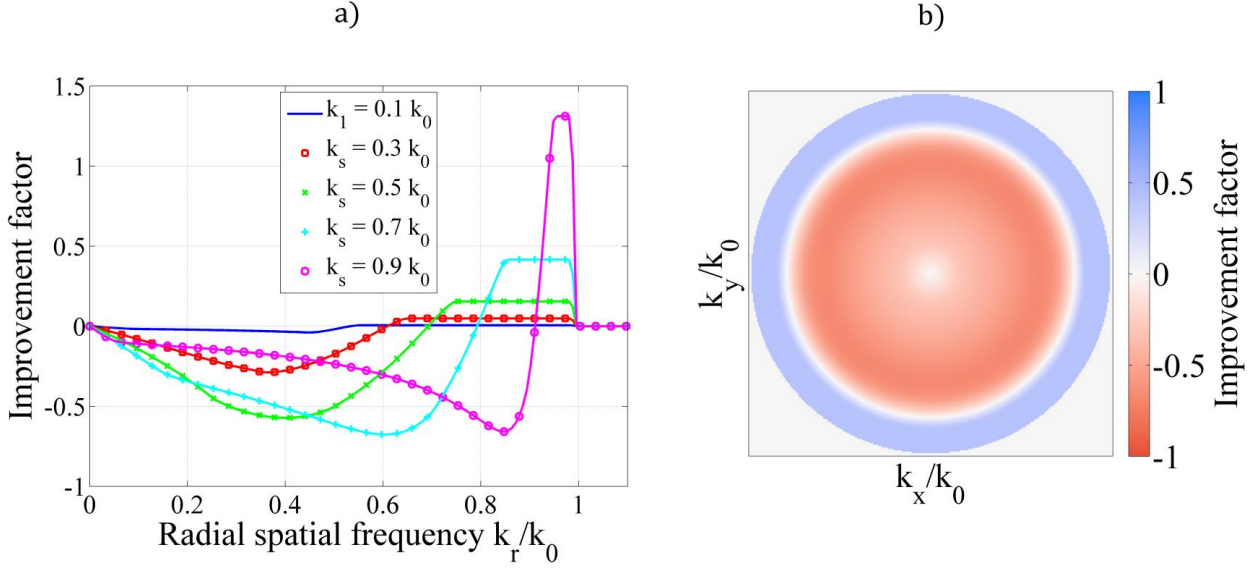


Figure S4 | Improvement factor for different radial splitting configurations. a) IF_{k_r} in dependency of the inner pupil radius k_s in a radial-mean plot. b) 2D-visualization of the improvement factor for a radial split with $k_s = 0.7 k_0$. Note the isotropic enhancement (blue color) of high spatial frequencies.

For noise normalized results (hence $\tilde{\sigma}_2^2 \leq \tilde{\sigma}^2 = 1$; and $\tilde{\sigma}_2^2$ being the noise variance of the outer ring sub-image) we find that increasing IF_{max} can be achieved by decreasing the width of the ring. Unfortunately in this case the enhancement can only be realized over a smaller region in k -space and the medium frequency losses generally increase as well.

The above introduced spatial frequency k_r' depends linearly on the inner pupil radius k_s , since the autocorrelation operation is linear in the sense that its output region of support is always double the input frequency limit, hence:

$$k_r' \propto k_s \quad (S28)$$

On the other hand the maximum improvement factor is inversely proportional to $\tilde{\sigma}_2$ (eq. S27), which is proportional to the number of photons present in the image formation (eq. S8). Hence IF_{max} is inversely proportional to the area of the outer ring sub-pupil, yielding in the following dependency on the squared inner pupil radius k_s :

$$IF_{max} \propto \frac{1}{k_s^2} \quad (S29)$$

From these two proportionalities (S28) & (S29) it can be seen that there is a tradeoff between either having a strong improvement (large IF_{max}) over a small region in k -space (small k_r'), or obtaining less enhancement (small IF_{max}) over a larger frequency region (large k_r').

This is exactly what is observed in figure S4 a), where the compromise used in this work is shown as the cyan curve. For the presented “proof-of-concept” experiment the idea was to have some detectable improvement over a larger region in k -space. Therefore both sub-pupils have been chosen (for our described experiment) to be of equal area, which lead to the inner pupil radius k_s :

$$k_s = k_0/\sqrt{2} \quad (S30)$$

S5 Comparison between measured and simulated point-spread-functions:

As is seen from eq. (S20), the weights of the weighted average recombination are the efficiency-normalized sub-OTF's. Those describe the optical system and are usually obtained by calculating the Fourier transform of the respective incoherent point-spread function (PSF) which is the absolute square of the coherent PSF:

$$a_r = f_A(NA; \lambda) \quad (S31)$$

$$h_r = |a_r|^2 \quad (S32)$$

$$\tilde{h}_k = \mathcal{F}\{h_r\} \quad (S33)$$

wherein f_A represents the Matlab function simulating an amplitude PSF with the numerical aperture NA and wavelength λ , according to [9]:

In our work the numerical aperture is given by the radius of the displayed phase distribution on the SLM (see Fig. 4 b). More precisely it is the sine of the pupil radius divided by the lenses focal length. Therefore the FP- NA and the inner SP- NA_1 are:

$$NA = \sin\left(\frac{226 \text{ px} \cdot 8 \frac{\mu\text{m}}{\text{px}}}{150 \text{ mm}}\right) = 0.012 \rightarrow h_r = f(0.012; 525\text{nm}) \quad (S34)$$

$$NA_1 = \sin\left(\frac{151 \text{ px} \cdot 8 \frac{\mu\text{m}}{\text{px}}}{150 \text{ mm}}\right) = 0.008 \rightarrow h_{r,1} = f(0.008; 525\text{nm}) \quad (S35)$$

The outer ring pupil PSF has been found by using the linearity of the Fourier transform and the fact that the outer ring pupil can be expressed as being the difference between full and inner pupil:

$$\tilde{a}_{k,2} = \tilde{a}_k - \tilde{a}_{k,1} \quad (S36)$$

$$a_{r,2} = \mathcal{F}^{-1}\{\tilde{a}_{k,2}\} = \mathcal{F}^{-1}\{\tilde{a}_k\} - \mathcal{F}^{-1}\{\tilde{a}_{k,1}\} = a_r - a_{r,1} \quad (S37)$$

$$h_{r,2} = |a_{r,2}|^2 = |a_r - a_{r,1}|^2 \quad (S38)$$

$$\rightarrow h_{r,2} = |f_A(0.012; 525\text{nm}) - f_A(0.008; 525\text{nm})|^2 \quad (S39)$$

Therefore the outer pupil PSF can be obtained via the absolute squared of the difference between full- and inner-pupil ASF using the same calculation routine.

The results of these calculations are shown in Fig. S5 for the three different sub-pupils, in a line plot along the horizontal direction as the solid red curve. For comparison also the different PSF's have been experimentally measured by putting a 5 μm pinhole at the sample position (see Fig. 4a) and subsequent capturing the corresponding images. The resolution limit Δx of our optical system (full pupil) can be estimated to be [3]:

$$\Delta x \approx \frac{\lambda}{2 NA} = \frac{525 \text{ nm}}{2 \cdot 0.012} = 21.88 \mu\text{m} \quad (S40)$$

Therefore the 5 μm pinhole is below the resolution limit and the corresponding image is expected to represent the system's PSF. The experimental results are shown as blue points in Fig. S5.

The pixel size in the simulation has been reduced from 2.2 μm (camera pixel size) to 2.15 μm due to the real optical system's magnification which differs from unity, the theoretically expected value for the $4f$ -system with equal focal lengths as shown in Fig. 4a.

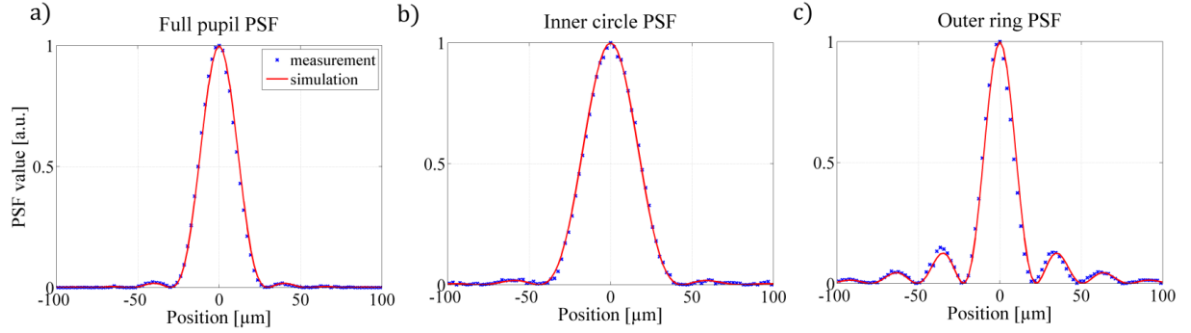


Figure S5 | Comparison between measured (blue points) and simulated (solid red line) PSF's for the three different sub-pupils. a) Full h_r . b) inner $h_{r,1}$ and c) outer pupil $h_{r,2}$ PSF. The simulations have been performed according to [10] and the procedure described in the text above. The simulated pixel size had to be reduced slightly by 2.3% to match the real imaging systems magnification, which was different from the expected magnification of one.

The magnification of the system has been measured using the width of the larger white square structure on the USAF-target. Its width is known from the manufacturer, which relates to an expected number of camera pixels. This number differs from the measured value (given as the full-width-half-maximum (FWHM) of the vertical line plot), the difference implies a de-magnification of the system by a factor of 0.977. The PSF-simulation was adjusted and the results are shown in Fig. S5. Both, measurement and simulated data fits very well.

Note that the calculated diffraction limit of $\Delta x \approx 22 \mu\text{m}$, matches the visually obtained limit shown with the yellow arrow in Fig. 5 & 7. The corresponding line group has a single line width of $\approx 11.05 \mu\text{m}$ and therefore yields a diffraction limit of $\Delta x = 2 \cdot 11.05 \mu\text{m} \approx 22 \mu\text{m}$.

S6 Profile line plots corresponding to the vertical line patterns to verify isotropy of the enhancement:

To confirm the isotropy in improvement of the applied radial splitting, also the line plots corresponding to the vertically aligned line structures are shown in Fig. S6.

Fig. S6 shows the experimentally obtained results. The depicted curves can be directly compared to those of Fig. 6 b & c of the main text.

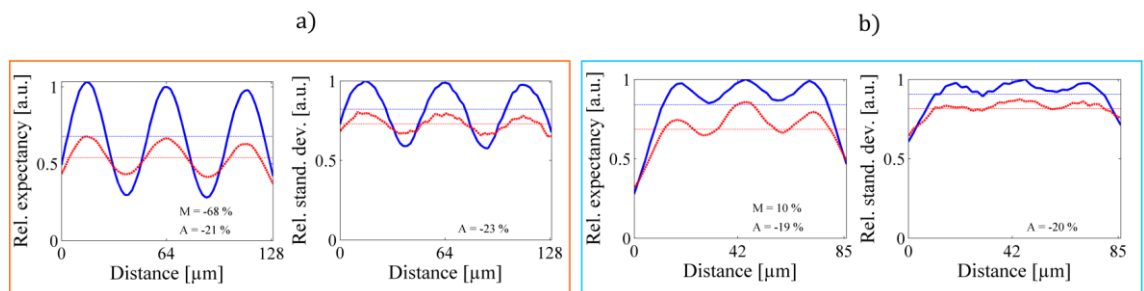


Figure S6 | Profile line plots for the vertical line structures of the experimental. For a detailed description see the figure legend of Fig. 6 in the main text. This line plots have here been generated by using the corresponding vertically aligned structures instead of the horizontal ones.

It is seen that the enhancement, which has been created using the split-pupil approach, does not change for the vertically aligned line structures of the USAF-1951 target, verifying the isotropy of the investigated radial split.

S7 Influence of a finite pattern structures on the average value:

In evaluating the different line plots of the FP- and SP-image results, we observed a difference in their average values (Fig. 6 b,c and Fig. S6 a,b). We attribute this to the USAF-target only consisting of finite semi-periodic structures with 3 bars.

The increase beam-skirt of the ring aperture leads to more intensity being transported to the previously dark regions around the 3-bars target, which not contributes to the average (see the simulation in Fig. S7 left column). In the case of an infinite extended bar structure (middle column) this effect does is not observed. Our simulations confirm our suspicion for the observed reduction of the average.

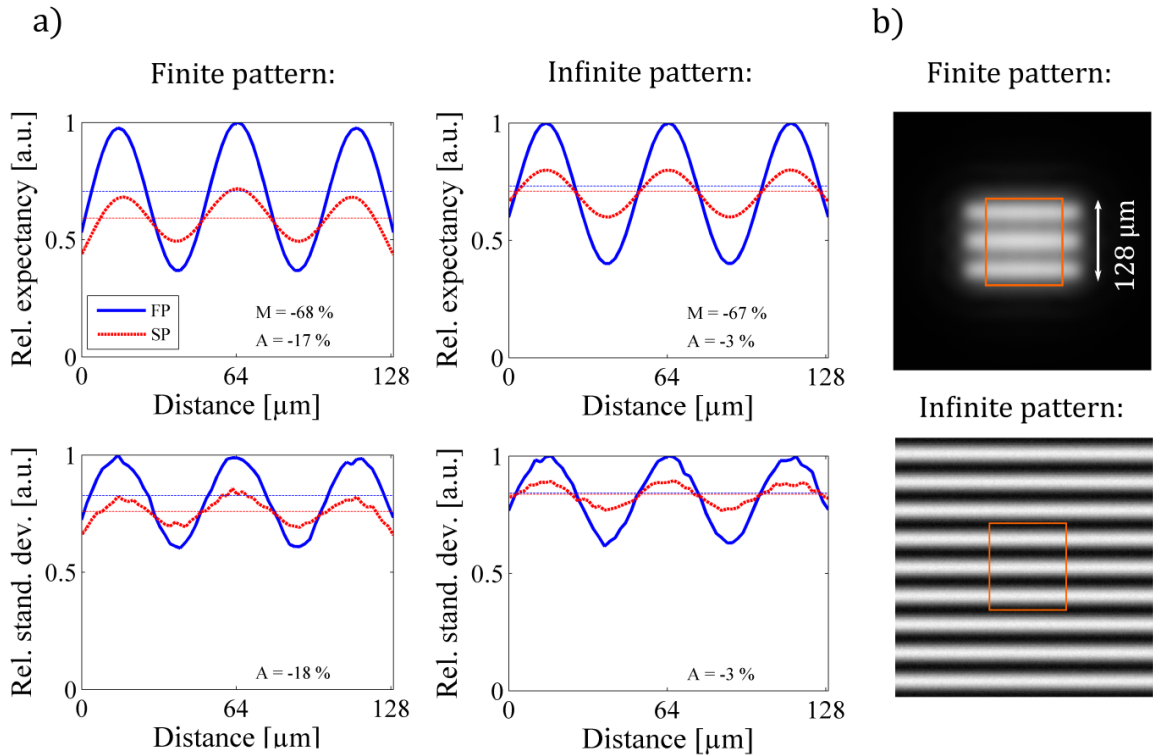


Figure S7 | Comparing the imaging performance between a finite & infinite periodic structure by simulation. Two different line structures; the bottom row is assuming an infinite structured, whereas the top corresponds to a finite structure similar to our experimental case (orange box) surrounded by zero brightness. **a)** shows the line plots similar to our experimental findings. **b)** depicts the corresponding simulated images.

S8 Theoretical evaluation of split pupil imaging for high NA objectives:

The intention of our work is to introduce the concept of split pupil imaging to the community, therefore we decided to keep it simple and used scalar theory for our theoretical investigation. For completeness we also present results corresponding to vectorial theory using [10].

Figure S8 shows simulation results for a high- NA objective with the following parameters:

$$NA = 1.4, \quad n = 1.518, \quad \lambda = 525 \text{ nm}$$

Comparing Fig. S8 a) and Fig. 3 b) (scalar case), it can be seen that both effective SP-OTFs look rather similar. But when obtaining the improvement factor (eq. S25), a clear difference is visible. In case of the vectorial theory, the improvement is very much enlarged. The maximum improvement factor $IF_{max} = 2.84 \gg 0.41$ (scalar case), has increased by one order of magnitude. The reason for this is that the importance of interference of light under high angles gets more important with increasing NA . Because our proposed SP approach promotes this interference (high angle = high spatial frequency), the benefit of employing split pupil imaging scales with the numerical aperture.

Figure S8 c) & d) show profile plots of the effective PSF of the system. A slight reduction of FWHM in the lateral and a rather strong increase in the axial direction can be observed. Later might be useful for extended-depth-of-field applications [16, 17] or fast volumetric imaging [18]. The axial elongation scales with splitting factor, which means: in the case of an equal area split (full pupil is divided into two equal sized sub-pupils) the effective PSF is elongated by a factor of two.

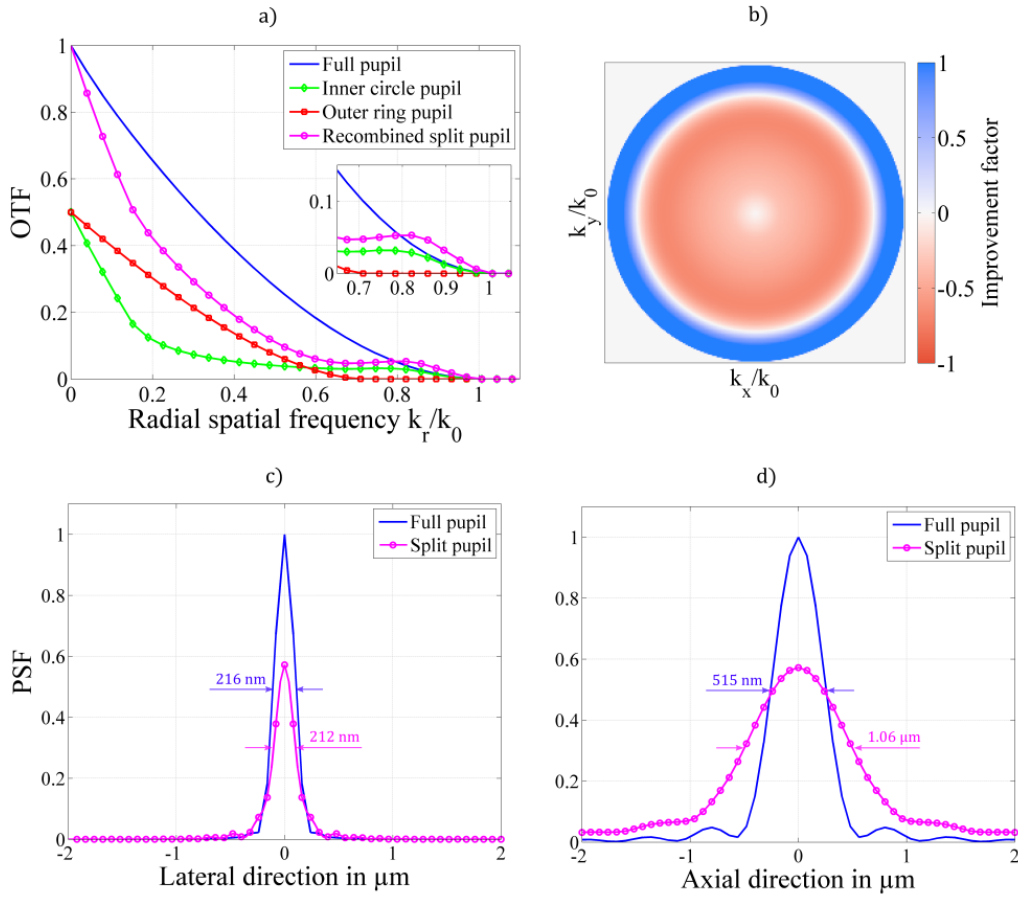


Figure S8 | Theoretical evaluation using vectorial calculation [10]. a) OTF comparison similar to Fig. 3 b) (scalar theory only). Both results visually look similar, but when calculating the improvement factor (b) we obtain a maximum improvement factor of $IF_{max} = 2.84 \gg 0.41$ (scalar case), which is one order of magnitude larger than in the scalar case (see Fig. S4 b). This shows that our proposed split pupil approach seems to be more advantageous for high- NA imaging systems. c) The corresponding effective PSF (magenta dots) provides a slightly reduced FWHM in the lateral direction, while suffering from a reduced peak value. On the other hand one observes an axial elongation (d), which might be useful for extended-depth-of-field applications [16, 17] or fast volumetric imaging [18]. Vectorial simulation for a microscope objective with: $NA = 1.4$, $n = 1.518$, $\lambda = 525$ nm.